

Rolling and Standing: A Low-Cost Curb-to-Cabin PM Monitoring Sensor Network for Sub-Saharan Africa

Nthenya Kyatha, Austin Bartlett, Jay Taneja, Richard Peltier

University of Massachusetts Amherst

Amherst, MA, USA

{mkyatha,asbartlett,jtaneja,rpeltier}@umass.edu

Abstract

Evidence for the air-quality benefits of bus electrification in Sub-Saharan Africa (SSA) is scarce, largely due to the high cost and complexity of long-term particulate matter (PM) monitoring. We present the architecture and design of OpenAQ-Transit, the *first unified curb-to-cabin air-quality monitoring network in SSA*. It is an open-hardware platform with two low-cost node types: a 15 W solar-powered bus-stop unit and a bus-mounted unit drawing from the vehicle power rail. Each node integrates **twin optical PM sensors** on staggered duty cycles for in-field drift tracking, **environmental channels** (temperature, humidity, pressure, sound) for context and correction, and a **PIR-triggered camera** for source attribution. Data are logged locally and uploaded via a cellular Notehub link supporting over-the-air firmware updates. Across 55 production units, this architecture enables low-maintenance, city-scale exposure mapping to evaluate the real-world impacts of diesel-to-electric bus transitions. In a 14-day BAM co-location, we calibrated 55 nodes, achieving < 15 % bias and 99% data-sync reliability while cutting PM sensor duty-cycle by 88 %. All hardware, firmware, and analysis scripts are open-source.

CCS Concepts

- Hardware → Sensor devices and platforms;
- Applied computing → Environmental sciences;
- Computer systems organization → Embedded and cyber-physical systems;
- Networks → Network monitoring.

Keywords

Air quality monitoring, Low-cost sensors, Internet of Things (IoT), Urban sensing, Transit-based monitoring, Sub-Saharan Africa, Smart city infrastructure.

1 Introduction

Road transport significantly contributes to air pollution in Sub-Saharan Africa (SSA), where over 70% of roads are unpaved or poorly maintained [9]. Consequently, diesel buses and minibuses, common in public transport, move slowly through traffic, resuspending dust and releasing exhaust particulate matter from their aging engines, further worsening pollution levels [8, 24].

Particulate pollution consists of two main size fractions: PM_{10} and $PM_{2.5}$. PM_{10} includes inhalable particles up to 10 micrometers in diameter, while $PM_{2.5}$ comprises finer particles 2.5 micrometers or smaller [1]. Studies have linked the inhalation of these particles to serious health issues [23], as both can penetrate deep into the lungs, with $PM_{2.5}$ potentially entering the bloodstream [1].

Prolonged exposure to $PM_{2.5}$ levels above the World Health Organization (WHO) daily guideline of $5 \mu\text{g m}^{-3}$ [25] significantly raises

cardiopulmonary mortality rates and childhood asthma prevalence. Alarmingly, over half of African countries report annual median levels exceeding $26 \mu\text{g m}^{-3}$ [26]. The situation worsens during weekday rush hours, with cities like Nairobi and Kigali often recording levels above $80 \mu\text{g m}^{-3}$ [19, 32], exceeding the WHO 24-hour limit of $15 \mu\text{g m}^{-3}$ [25]. Chronic traffic congestion forces commuters to wait at curbside stops and spend long periods in poorly ventilated buses, increasing their exposure to $PM_{2.5}$. This exposure is linked to higher rates of bronchitis, asthma, and cardiovascular diseases in the region [23, 28]. However, data at the street level is limited due to the high costs of dense monitoring networks.

To address the data gap, we propose low-cost optical sensors for mass transit in Sub-Saharan Africa, but three challenges need to be tackled. First, evaluations are typically conducted in controlled settings, ignoring factors like vibration, heat, and dust found on local roads[18, 21, 22]. Second, most prototypes often require continuous power and broadband connectivity, which can be unreliable in remote areas [3, 8, 24]. Lastly, research often separates bus-stop and in-vehicle sensing, leading to a lack of integrated systems that track exposure from curb to cabin [6, 16, 17]. The question remains: Can we develop a robust, low-cost sensor platform that can withstand the conditions of African roads while continuously capturing $PM_{2.5}$ exposure from curb to cabin during real-world transit operations?

In this paper, we describe the system design, implementation, and evaluation of OpenAQ-Transit, a **dual-mode air-quality monitoring node** designed to operate both at bus stops and on board buses, representing the **first unified exposure network in SSA**. The static nodes are solar-powered and pole-mounted, while mobile nodes utilize bus power. Each unit features **twin optical PM sensors** that measure $PM_{1.0}$ and $PM_{2.5}$ on staggered duty cycles, facilitating drift checks in the field (section 4.3.2). Additional sensors monitor temperature, humidity, pressure, and sound, supplying covariates for humidity correction and contextual analysis. **Over-the-air (OTA) capabilities** enable operators to adjust sampling rates and perform firmware updates remotely, reducing site visits and keeping the fleet adaptable as conditions evolve (section 4.3.4). A **PIR-triggered camera** captures images on motion detection to attribute PM spikes to potential sources. Together, these features support scalable, low-cost monitoring to quantify the environmental benefits of electrifying urban bus fleets.

We will roll out a total of 55 nodes, comprising 25 solar-powered bus stop units and 30 bus-mounted units, across Nairobi and Kigali, beginning in August 2025 and continuing for two years. This dataset will enable transport agencies to assess reductions in $PM_{2.5}$ from electric buses, pinpoint areas for dust mitigation, and establish low-emission zones. Additionally, civil society partners will be able to utilize these insights to promote clean-fleet incentives and enforce stricter idling regulations. Furthermore, all hardware, software, and

analysis tools will be made available under permissive licenses following the first public data release in Q4 2025, thus supporting replication efforts by NGOs and citizen-science organizations.

The proposed approach contributes to the design and implementation of similar systems in several significant ways:

- **Dual-mode hardware.** A single low-cost node operates at curb-side stops (solar) *and* on board buses (vehicle power), creating the first unified exposure network in SSA.
- **Resilient OTA software.** Run-time variables and complete firmware images can be updated wirelessly; the modem can queue data for 30 days, ensuring that schedules and code remain intact during power or backhaul outages.
- **In-field drift tracking.** Twin optical PM sensors operate on staggered duty cycles, allowing continuous calibration drift analysis without the need for external references (section 6.2).
- **Open access.** All PCB files, software, and analysis notebooks will be released under permissive licenses after the initial data release in Q4 2025.

2 Literature Review

The advent of low-cost particulate matter sensors, cloud-connected microcontrollers, and affordable solar technology has rendered dense air-quality networks both technically and financially viable. Previous research can be divided into four main areas that provide context for this study: (i) power management in existing IoT sensing platforms, (ii) reliability and maintenance in low-cost PM sensors, and (iii) deployments in transit-oriented and African contexts.

2.1 Power Management in Existing IoT Sensing Platforms

Power management in Internet of Things (IoT) sensing platforms is crucial for operational efficacy, especially in air quality monitoring systems. While low-cost sensor nodes can reliably stream air-quality data, their energy budgets, which impact longevity and deployment, have been insufficiently addressed.

Existing platforms provide insights into this issue. Stationary and phone-tethered designs, like AirCloud, transmit data over Ethernet for fixed installations and via Bluetooth for portable use, yet fail to report sensor or communication energy consumption, assuming a constant power supply [5]. This reliance makes autonomous and solar-powered operation impractical.

Second, vehicular sensor networks (VSNs) such as OpenSense Zurich bolted a 4.5 kg Gumstix node to trams; each station drew \approx 40 W from the traction supply, rendering battery or solar power impractical [20]. MAQUMON buffered ozone, CO, and NO₂ locally and uploaded only near Wi-Fi hotspots [33], while another VSN texted CO₂ readings over GSM using the vehicle's 12 V line [10]. Although VSNs widen spatial coverage, their dependency on vehicle power restricts deployment to motorised fleets and excludes roadside or off-grid contexts.

Furthermore, an analysis of commercial low-cost monitors, including the Edimax AirBox and PurpleAir II-SD, reveals that these devices require external power adapters and operate at fixed sampling rates [7, 27]. In practical deployments, such as a 30-day international campaign, PurpleAir units were powered using portable

power banks, necessitating manual retrieval of data on a weekly basis [3]. While firmware updates are done over-the-air, these devices don't adjust sampling rates based on battery status, and the twin lasers mainly provide redundancy without compensating for drift.

Power management in academic prototypes and commercial devices often relies on stable power sources, which do not suit regions with low grid reliability, like SSA. We propose adaptive power budgeting strategies such as solar charging, battery-aware duty cycling, and over-the-air configurations. These strategies aim to optimize sensing resolution and energy use, enhancing the sustainability of IoT sensor deployments in resource-constrained environments.

2.2 Reliability & Maintenance in Low-Cost PM Sensors

Energy autonomy alone is insufficient if the measurements themselves drift out of specification. Field studies have revealed significant long-term uncertainty. During the eight-month CAIRSENSE campaign, replicated optical PM sensors exhibited nearly perfect correlation with one another ($r \approx 0.99$), yet only moderate correlation with the federal reference monitor (FRM, $r \approx 0.65$). Even after adjustments for temperature, relative humidity, and sensor age, the median drift remained approximately 15% [15]. Sousan et al. observed vibration-induced offset shifts of roughly 5% per 1,000 km along bus routes, whereas Maag et al. associated high sampling rates with accelerated aging [22, 30].

Current mitigation strategies, such as adaptive duty cycling and periodic zero checks, rely on mains power [4, 21]. They consequently fail during the multi-day grid and cellular outages that are common in Nairobi and Kigali. To date, there have been very few published platforms that co-locate two optical engines on a single board for *real-time* drift tracking, especially in SSA. Our dual-sensor architecture integrates twin PM engines, staggers their duty cycles to quantify drift *in situ*, and pushes updated sampling rates over-the-air without requiring a site visit and within the adaptive power envelope defined in Section 2.1.

2.3 Transit-oriented and African Deployments

Public transit systems tend to concentrate both passengers and pollution; however, they remain relatively under-researched, particularly in sub-Saharan Africa (SSA). Initial transit trials highlight the challenges involved. Kaivonen and Ngai equipped Helsinki buses with PMS5003 sensors, achieving a spatial resolution of 30 meters, but depended on nightly depot charging to power the batteries [16]. Salama et al. reported PM_{2.5} peaks of approximately 95 $\mu\text{g m}^{-3}$ at bus terminals in Saudi Arabia, while SenseVair integrated low-frame-rate imagery with particulate matter readings to identify pollution spikes [29, 38]. However, each study presupposed easy access to grid power or regular maintenance.

In the African context, Awokola's network of 13 fixed PurpleAir stations provides essential baseline data but lacks mobility [3]. To our knowledge, there has been very limited, if any, published research that simultaneously monitors curbside and onboard PM levels along bus corridors in East Africa, where diesel and emerging electric fleets frequently share congested roadways.

Our proposed system comprises 55 dual-mode sensor nodes: 30 solar-powered units designed for bus stops and 25 dashboard-powered units intended for onboard vehicles. These sensors will be deployed in Kigali and Nairobi, facilitating the creation of a high-resolution exposure map that captures both roadside and in-vehicle environments along East African bus routes. Furthermore, this data will aid in identifying pollution sources from diesel and electric vehicle fleets and will inform targeted transit strategies to enhance air quality in urban areas.

2.4 Remaining Gaps

- (1) **Durability:** Can twin sensors stay accurate amidst vibration, heat, and dust in bus environments, and can we monitor their drift over time?
- (2) **Autonomy:** Can the system tolerate multi-day power and backhaul outages while continuing to log and recover data?
- (3) **Unified coverage:** Can one platform capture both curbside and on-bus PM exposure, adapting its operation to solar or vehicle power with OTA control?

3 System Design

To close the gaps articulated in §2.4, we designed OpenAQ-Transit. It is a unified sensing platform that operates consistently at bus stops and on moving buses, ensuring data comparability. Its architecture follows four key principles: (i) each node is programmed once during assembly, with only run-time parameters adjusted remotely, preventing configuration drift; (ii) a power-aware scheduler allows solar-powered nodes to function for at least 48 hours without sunlight; (iii) an integrated health module monitors battery, temperature, signal strength, and sensor bias, enabling reactive maintenance; (iv) all readings are locally cached and transmitted over a secure TLS connection once connectivity is restored, safeguarding against data loss during disruptions. Section 5 evaluates these design requirements through Objectives **O1–O4**.

3.1 Layered Node Architecture

Each node consists of three parts (see Fig. 1a). The *sensor plane* includes optical particle counters, a temperature, humidity, and pressure capsule, a PIR motion sensor, an acoustic microphone, and a low-power camera, all powered by a 5 V supply. The *control plane* features a low-leakage microcontroller and a sensor-hat PCB for increased GPIO capacity, along with an I²C/SPI multiplexer to avoid address conflicts. This plane also has removable non-volatile storage and a real-time scheduler for timestamps and duty cycles. The *back-haul plane* combines a dual LTE/Wi-Fi modem with GNSS and a persistent message queue for encrypted cloud data transmission, capable of buffering data for thirty days during outages. This design allows Phase I tests (**O1, O2**; section 5, section 6.1) to focus on the sensor plane, while Phase II fault injections (**O4**; section 5, section 6.4) address control and back-haul logic.

3.2 Mode-Driven Operation

At startup, nodes enter either *Bus* or *Stop* mode. In *Bus* mode, continuous dashboard power allows for sampling PM and environmental channels every ten minutes and hourly back-hauling. In *Stop* mode, GPS fixes last several hours, and PIR-gated imaging is utilized, with

radio communication windows adjusted based on battery state-of-charge (SoC). Nodes can be repurposed by switching modes through the cloud console. This dual-mode framework supports the “low-cost curb-to-cabin” initiative, validated through drive tests and solar deep-discharge scenarios.

3.3 Power-Aware Scheduler

Runtime energy management operates through a two-stage process, as depicted in Fig. 1b. First, a scheduler checks if a task’s nominal interval has passed. Then, a SoC governor decides whether to extend or deny the task based on the battery table (Table 5). If energy is low, the node first disables imaging, then throttles cloud synchronization (both upload and download) and GNSS fixes. Finally, it extends the core PM-sensing window to protect key drift tracking data. The deep-discharge test (**O4**) shows that GPS and synchronization rates degrade and recover as expected.

3.4 Edge–Cloud Data Pipeline

During each polling window, the controller aggregates channel readings into a single JSON record and queues up to ninety-five records. Uploads occur when the queue is full or an energy-aware timer triggers. The cloud relay adds location metadata, archives the payload, streams it for analytics, and checks alert rules based on battery voltage, temperature, humidity, signal strength, and backlog depth. Email alerts with the latest GPS fix are sent if any thresholds are exceeded. Cold-soak and network-blackout tests detailed in section 6.4 confirm timely alerts and zero data loss.

3.5 Reliability and Maintainability

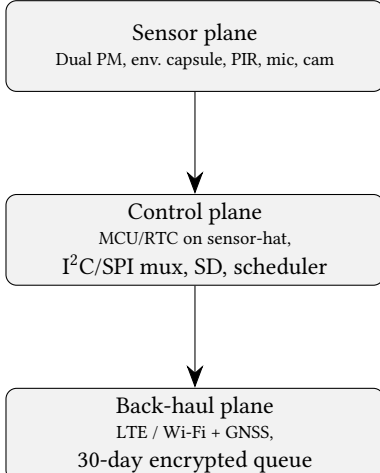
Twin particle counters use staggered duty cycles to track their mutual bias in situ and facilitate drift analysis without external references. When the node synchronizes, it adds a health footer with battery voltage, MCU temperature, cellular RSSI, and queue depth for server-side alerts. Peripherals and sensors connect via plug-and-play headers, allowing easy on-site module replacements. Stage-I tests (**O2–O3**) show the twin-sensor strategy maintains $\pm 10 \mu\text{g m}^{-3}$ repeatability over fourteen days. Stage-II cold-soak tests (**O4**) confirm that low-temperature alerts trigger within about half an hour after a fault.

3.6 Open Access

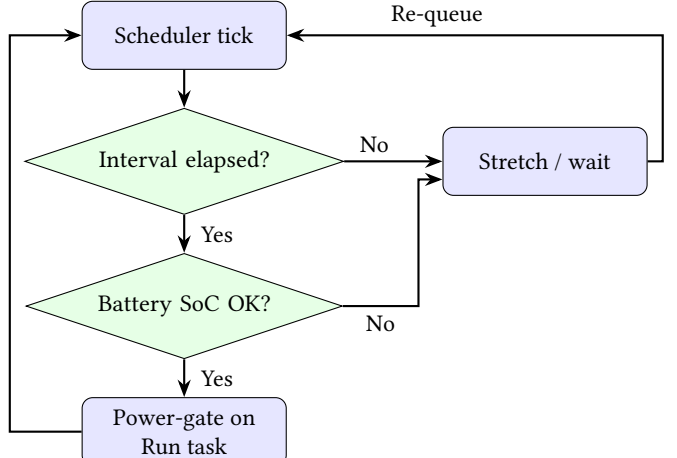
To enhance reproducibility, all relevant materials, including the complete PCB layouts, software, and calibration scripts, are made available under permissive licenses. External teams can therefore replicate the chamber protocol used for **O1–O3** or adapt the SoC-aware scheduler to other solar-powered deployments.

4 Implementation

The three-plane architecture, mode profiles, and two-stage energy gate in section 3 state *what* every node must achieve. This Implementation section shows *how* we realise those abstractions. We begin with a system-level prototype overview in section 4.1 and then discuss the Hardware Stack, controller sandwich, sensor-hat, communications, storage, power, and enclosure in section 4.2. Section 4.3 covers the Software & Runtime layer for scheduling, health monitoring, and OTA control. Finally, section 4.4 addresses power



(a) Layered node architecture



(b) Two-stage power-aware runtime

Figure 1: High-level system diagrams for OpenAQ-Transit: (a) three-plane node architecture; (b) battery-aware task scheduler.

efficiency and adaptability under varying energy conditions, while section 4.5 details the health-monitoring framework and alerting mechanisms for detecting and responding to faults.

Table 1 maps each design principle to its concrete realisation.

Table 1: From design abstraction to concrete realisation

Design primitive	Implemented by
Sensor plane	Sensor-hat PCB, plug-and-play headers
Control plane	Swan MCU + RTC, I ² C/SPI mux, μSD
Back-haul plane	LTE/Wi-Fi modem with GNSS, 30-day queue
Mode profiles	'env.var' flags: <i>Bus</i> vs. <i>Stop</i>
Two-stage energy gate	Scheduler loop + SoC governor in software
Health monitoring	Battery/Temp/RSSI footer on every sync
Loss-proof pipeline	95-record JSON batches, TLS upload

4.1 Prototype Architecture

Figure 2 presents a block diagram illustrating the selection of components for the sensor modules, controller, communications, storage, power, and support components. Figure 3 showcases a 3D rendering of the system, highlighting both the internal and external views.

4.2 Hardware Stack

4.2.1 Controller. We use the Blues Swan v3.0 microcontroller unit (MCU)[34]. It features an STM32L4R5 microcontroller that operates at 120 MHz and is based on the Cortex-M4 architecture. It includes 2 MB of Flash memory and 640 kB of RAM. This advanced board offers a variety of connectivity options, including four I²C buses, three SPI ports, and a few general-purpose input/output (GPIO) pins, facilitating robust communication with various peripherals. Additionally, it is equipped with a real-time clock (RTC) for precise

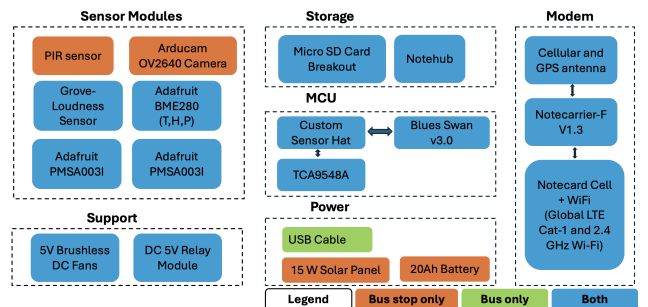


Figure 2: Block diagram of the monitoring kit: (i) Sensors: fan, relay, PIR, camera, loudness, BME, dual PM-AQI; (ii) Storage: SD logger and Notehub gateway; (iii) Controller: Blues Swan MCU with custom sensor hat; (iv) Communication: Notecarrier F and Notecard cell/WiFi with GPS; (v) Power: solar with battery or bus dashboard.

timekeeping and employs a 2 A regulator for efficient power management. It consumes minimal power in deep sleep mode, approximately 8 μ A, making it an excellent choice for battery-operated devices. Most sensors in section 4.2.2 utilize either I²C, SPI or both. To address address conflicts among devices, an I²C multiplexer (TCA9548A) [13] is added to the custom sensor hat.

4.2.2 Sensor Module. Each node is equipped with two Adafruit PMSA003I PM sensors [14] that utilize Plantower PMS5003 technology. They provide real-time mass concentrations in both standard and environmental units, as well as particulate matter count per 0.1L of air. For environmental sensing of temperature, humidity, and pressure, the low-cost Bosch BME280 sensor [12] is chosen. This is because it measures humidity with $\pm 3\%$ accuracy, barometric pressure with ± 1 hPa absolute accuracy, temperature with $\pm 1^\circ$ C

accuracy and altimeter with ± 1 m accuracy making it appropriate for our use case.

The Grove analog loudness sensor [31] is used to measure ambient noise. It features an amplifier based on LM2904 and a built-in microphone that amplifies and filters high-frequency signals to produce a positive envelope output, directly proportional to the sound level. To reduce signal disturbances, the input is filtered twice within the module. A PIR motion sensor and an ArduCAM OV2640 camera [2] are used for capturing images. The camera supports JPEG compression, single/multiple shot modes, one-time capture, burst read operations, and low power mode, which is crucial for our application.

4.2.3 Communications Module. A three-board Feather-format stack integrates the Swan MCU, a Notecarrier-F base [35], and a NOTE-WBGL modem [36]. The Notecarrier-F facilitates connections for both the modem and microcontroller, while also housing a SIM card holder for local services. The NOTE-WBGL Notecard offers a combined global LTE Cat 1 service, complemented by a 2.4 GHz Wi-Fi fallback option. Additionally, it features built-in GNSS and an accelerometer, along with a pre-provisioned eSIM that offers 10 years or 500 MB of service. The Swan MCU communicates with the Notecard via UART, efficiently batching and uploading data to the Blues Notehub through both cellular and Wi-Fi connections, while also incorporating location information obtained from GNSS or cellular triangulation. To enhance both cellular and GPS reception, the kit includes a dual LTE + GNSS FPC antenna with a u.FL connector, covering frequency ranges from 698 MHz to 4 GHz.

4.2.4 Storage Module. The Adafruit MicroSD Card breakout module [11], equipped with a 64 GB microSD card, serves as the local storage. For cloud storage, the Blues Notehub site [37] is utilized. Additionally, the Notecarrier F enables local data queuing for a specified duration; for further details on queue depth and retry logic, please refer to section 4.3.3. Notehub also supports configurable forwarding destinations, such as Google Cloud Pub/Sub, Amazon S3, or any standardized HTTPS endpoint, thereby enhancing data integrity and reliability across various operational scenarios.

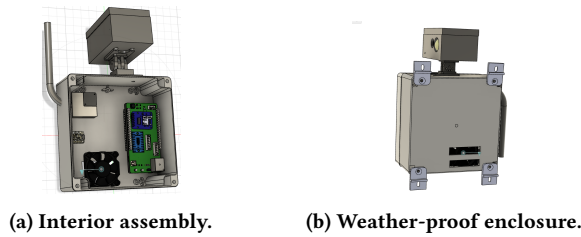


Figure 3: Environmental monitoring unit: (a) Interior layout with PCB, fan, sensors, and airflow path; (b) enclosure with dual-sensor pod and mounting pins.

4.2.5 Power Module. The Notecarrier automatically switches between solar, Li-ion, and USB power sources. Fixed bus-stop nodes receive 5 V from a 15 W / 20 A h solar kit, which has been sized based on two-week discharge tests (see Table 2). Mobile nodes draw power directly from the USB outlet on the dashboard. If needed,

the Notecarrier F can also manage solar charging for connected batteries.

Table 2: Solar-battery budget for a bus-stop node

Parameter	Value	Rationale
Worst-case load	0.32 A @ 5 V	Overnight discharge tests
Daily energy draw	38 Wh d ⁻¹	0.32 A \times 24 h
Adjusted requirement	59 Wh d ⁻¹	66 % conversion efficiency
Required panel power	12 W	59 Wh \div 5 h full sun
Selected panel	15 W @ 5 V	25 % weather head-room
Required battery cap.	13 A h	Includes losses, 80 % DoD
Selected battery	20 Ah @ 5 V	\approx 2 days autonomy

4.2.6 Enclosures. The system is housed in waterproof IP-rated plastic enclosures as shown in Fig. 3. The main enclosure protects essential components like PM sensors, environmental sensors (temperature, humidity, pressure), MCU, communication modules, and local storage. A secondary enclosure contains auxiliary elements such as a camera, motion sensor, and noise sensor. Airflow is maintained via a short intake tube, with a relay-controlled fan expelling stale air before sensor readings. Both enclosures ensure durability and protection from harsh weather, while optimizing airflow for the PM sensors.

4.3 Software & Runtime

To facilitate effective monitoring at bus stops and within buses, the software employs a mode-specific initialization sequence along with an energy-efficient, time-scheduled sensor polling loop. This design optimizes the balance between data collection and power consumption.

4.3.1 Mode Profiles. At start-up, the MCU operates in either *Bus* or *Stop* mode, depending on its location. Each mode consists of a set of parameters that govern the scheduler's sensor polling, GNSS fixes, and synchronization intervals. All parameters can be remotely modified through Notehub using env.var.

Table 3: Radio and GPS cadence for the two-mode profiles (OTA-tunable). Upload = outbound data \rightarrow cloud, Download = inbound config \leftarrow cloud. The stop-node timings are further stretched or shrunk by the SoC table below.

Mode	Upload	Download	GPS fix	Camera
Bus	60 min	60 min	5 min	off
Stop	5 h (SoC)	2 h	8–48 h	PIR+10 min hb

4.3.2 Sensor Polling Strategy. The sensor polling schedule is divided into two categories: general sensing and reliability monitoring of sensors. Every ten minutes, a four-minute *general window* opens, during which core sensors take readings once per minute. Additionally, every four hours, a 30-minute *reliability window* is activated, keeping one of the twin PM sensors active for drift tracking. This staggered schedule supports the drift-analysis experiment in section 6.2.

The camera is activated whenever the PIR sensor detects motion. If no motion is detected for 30 minutes, a heartbeat (hb) image is captured every 10 minutes. Hence, PM spikes are correlated with images taken within a margin of ± 2 minutes and are manually tagged for pollution sources. The specific default intervals are in Table 4.

Table 4: Sensor and camera cadence (default values, OTA-tunable). “Burst” shows the duty cycle inside each interval.

Channel	Interval	Burst	Purpose
AQI ₁	10 min	4×1 min	PM _{1.0} , PM _{2.5} baseline
AQI ₂	4 h	30 min	drift study
Env. sensors	10 min	4 × 1 min	Temp / RH / P / Noise
GPS (bus)	5 min	single fix	Route alignment
GPS (stop)	8–24 h	single fix	location reference
Camera	PIR + hb	JPEG	source ID

4.3.3 Data Synchronization. Readings collected within a specific window are combined into a JSON object and queued on the Notecard using a preset template(*note.template*). The Notecard can buffer up to 95 objects per session. During synchronization, it connects to Blues Notehub via cellular or Wi-Fi, and if the connection fails, the data is stored in flash memory until successfully sent. After uploading, the MCU compresses the relevant CSV rows on the SD card. The application adapts data transmission to Blues Notehub based on available energy, queuing unsent messages for up to 30 days during poor network coverage. It ensures messages are delivered in the correct sequence once connectivity is restored and optimizes payloads by removing unnecessary JSON fields and standardizing units.

4.3.4 Remote Configuration. The system enables remote reconfiguration using Notecard environment (`env.var`) variables, allowing for real-time adjustments to settings such as synchronization intervals for cloud data and camera activation conditions, all without requiring physical access or rebooting. Additionally, full firmware images can be delivered through the same channel, facilitating bug fixes and the rollout of new features. This approach enhances reliability and reduces maintenance costs.

4.3.5 System Health Monitoring. The synchronization mechanism serves a dual purpose, acting both as a means of data transmission and a health-monitoring tool. It logs internal diagnostics while maintaining consistent communication with the Blues Notehub platform. During each data sync, the sensor kit uploads key metrics, including battery voltage, MCU temperature, cellular signal strength, and note counts. By analyzing these metrics during synchronization, we can detect potential hardware failures, power issues, or connectivity problems before they impact data collection. Additionally, alert conditions are established to flag nodes that fall outside of nominal ranges, leading to the issuance of maintenance alerts along with node IDs and their respective locations.

4.4 Power Considerations

Effective power management is crucial for solar-powered bus stop units, given the fluctuations in energy availability due to environmental conditions. All electronics, therefore, run from a regulated 5 V rail whose deep-sleep draw is below 10 μ A.

4.4.1 Duty-cycled sensing. Sensors are activated only during the designated polling window. This approach collects essential data while allowing the system to enter a low-power mode, thereby conserving energy. High-power components, such as the camera and fan, are turned on only when necessary.

4.4.2 Event-driven imaging. The camera is activated either by PIR motion detection or at predetermined intervals. This method reduces power waste by limiting unnecessary image captures, ensuring relevant images are taken during times of increased activity.

4.4.3 Adaptive configuration. The system monitors its battery voltage to optimize energy consumption and extend battery life. The voltage is mapped to five SoC bands based on set thresholds. GPS and data transmission rates for both outbound sync (data \rightarrow cloud) and Inbound sync (conf. \leftarrow cloud) are lengthened as the battery pack empties, especially during periods of low solar exposure. As a result, the system can operate autonomously for extended periods without manual adjustments. Table 5 lists the voltage thresholds for each SoC band together with the corresponding GPS-fix intervals and outbound/inbound sync rates

Table 5: SoC-dependent back-haul throttling for stop nodes. GPS = time between fixes; “disabled” means the GPS is kept off to save power.

SoC band	Threshold	GPS	Outbound	Inbound
USB	4.6 V	8h	5h	2h
High	3.8 V	12h	8h	4h
Normal	3.1 V	24h	5h	2h
Low	2.0 V	48h	12h	8h
Dead	0 V	disabled	24h	24h

4.5 Alerts

Each payload comprises a Notecard status block that reports battery voltage, board temperature, cellular RSSI, and the number of queued notes. The system continually monitors these fields and generates an email alert when any thresholds are exceeded. If the battery voltage drops below the “low” state of charge (SoC) threshold (section 4.4.3), a `<deviceUID>_LOW_BATT` alert is triggered, where `deviceUID` is the device’s unique ID. Furthermore, if the board temperature falls outside the range of 15°C to 45°C, a `<deviceUID>_LOW_TEMP` alert is issued for temperatures below 15°C, and a `HIGH_TEMP` alert is issued for temperatures above 45°C. An alert for `<deviceUID>_LOW_HUMID` or `<deviceUID>_HIGH_HUMID` is generated when BME280 humidity levels fall below 20% or exceed 70%, respectively, for 30 minutes or more. Lastly, when the RSSI is below 1 bar for 12 hours, there are over 190 notes, or there’s no contact for 24 hours with normal and above battery voltage (5), a `<deviceUID>_COMMS_FAIL` alert is triggered. In response to thermal

alerts, the relay-controlled fan cools the enclosure while the sampling schedule remains unaffected. All thresholds are configurable over-the-air (OTA).

5 Evaluation

This evaluation co-locates production OpenAQ-Transit v1.0 nodes with a beta-attenuation monitor (BAM), which serves as the reference instrument for measuring $\text{PM}_{2.5}$ mass concentration. The evaluation is structured around four primary objectives: (**O1**) to quantify $\text{PM}_{2.5}$ bias and limits of agreement against the BAM following a one-time chamber calibration; (**O2**) to ensure that sensors remain within the $\pm 10 \mu\text{g m}^{-3}$ repeatability band over time; (**O3**) to monitor calibration drift of the twin PM sensors operating at varying duty cycles; and (**O4**) to assess system robustness under conditions of power, connectivity, and environmental stress.

Stage I : Chamber performance tests (O1, foundation for O2 & O3). All 55 nodes were installed in a chamber alongside the BAM and underwent a series of 48-hour clean–burst–purge cycles over 14 days. During the clean phases, clean air was introduced into the chamber to establish zero offsets, while the dust bursts introduced pollution, allowing for the determination of span gains k . These measurements address objective **O1** by quantifying $\text{PM}_{2.5}$ bias and limits of agreement relative to the reference monitor. The resulting pairs of offset, k also set a baseline necessary for monitoring long-term stability and drift, as addressed in objectives **O2** and **O3**. During recovery phases, clean air is reintroduced to observe how long it takes for the sensors to return to baseline readings. Should the second offset differ by more than $> 2 \mu\text{g m}^{-3}$, the stored offset is adjusted to the mean of the two measured values.

Stage II : Stress and robustness tests (O4, supports O2 & O3). During this phase, we conducted fault injections on one solar-powered node and three randomly selected USB-powered nodes to assess fleet resilience. The deep-discharge test exposed the solar kit to prolonged darkness until it hit the Low State of Charge (SoC) threshold, verifying the automatic adjustment of GPS and synchronization rates (see Table 5). We monitored recovery once sunlight was restored. In this scenario, the durations for GPS fixes were temporarily updated for the various SoC bands: 10 minutes for High, 15 minutes for Normal, 25 minutes for Low, and 45 minutes for Dead. The software was also updated to send notifications about changes in voltage SoC bands that impacted GPS fixes and synchronization times, alerting us via phone and Notehub.

The cold-soak test exposed the kits to 5°C to trigger low-temperature alerts below 15°C , validating the health-monitoring pipeline. OTA re-tuning was performed through Notehub, extending the sensor window from 4 to 5 minutes without re-flashing. We also updated the Notecarrier's firmware and activated text message notifications and Notehub records.

The three USB-powered kits were evaluated in a moving vehicle across regions with low cellular coverage to verify the accuracy and stability of the GPS, as well as to assess the modem's data queuing during outages (objective **O4**). Cloud synchronization was temporarily configured to occur every 15 minutes for both outbound and inbound data. Additionally, the vehicle was parked in a low

coverage area for 35 minutes to simulate data queuing, coinciding with two synchronization sessions.

6 Results and Discussion

6.1 Stage I: Calibration and Fleet Accuracy

Figures 5 and 4 present the results for the power-up, clean air, durst burst, and recovery phases for one of the sensor kits. Similar trends are observed across all sensor kits, with values staying within ± 3 of each other. BAM data was collected hourly, while OpenAQ-Transit collected data every minute. Therefore, we resampled our sensor data to an hourly format before proceeding with further analysis.

Clean-air agreement (November 25, hourly means). During the 24-h background period $\text{PM}_{2.5}$ never exceeds $7 \mu\text{g m}^{-3}$. Absolute accuracy remains high ($\text{MAE} = 2.8 \mu\text{g m}^{-3}$; 95% of points within $4.8 \mu\text{g m}^{-3}$ of the BAM), even though the Pearson correlation is statistically insignificant ($r = -0.09$, $p = 0.68$), a common outcome when both series hover at the sensor's counting limit. A baseline-only span fit gives $k \approx 2.50$; we record this value for completeness, but continue to apply the burst-derived span to all field data.

Dust-burst response (December 02, hourly means). Both instruments capture the dust plume that starts at 14:50 and peaks in the 15:00–16:00 bin. Shape agreement is excellent ($r = 0.981$, $p < 3 \times 10^{-17}$); $\text{MAE} = 11.5 \mu\text{g m}^{-3}$ and 95% of points lie within $34 \mu\text{g m}^{-3}$. A span coefficient of $k = 1.54$ corrects the raw sensor's 35% under-estimate, aligning the peak within $\pm 5\%$ of the BAM while preserving the common 20-min e-folding decay observed across all 55 kits.

Post-purge recovery (December 03, hourly means). After the purge, concentrations fall to $2\text{--}11 \mu\text{g m}^{-3}$. The sensor maintains $\text{MAE} = 4.9 \mu\text{g m}^{-3}$ and 95% $|\Delta| < 8.1 \mu\text{g m}^{-3}$, despite the lower correlation ($r = 0.699$, $p = 1.5 \times 10^{-4}$) characteristic of near-blank conditions. All 55 kits exhibit the same recovery with a median $\tau = 11.0 \pm 1.3$ min, well inside the 15-min dwell time required for roadside deployment.

Across the 55-kit ensemble, the low-cost optical sensors (1) reproduce BAM timing to within one sampling interval, (2) maintain a span error $< 15\%$ after calibration, and (3) return to baseline within the 15-minute dwell time expected between successive roadside deployments thereby fully meeting objective **O1**. These results confirm that the mass conversion and span coefficients derived from the representative kit are valid for the entire production batch.

6.2 Twin-sensor Agreement (O2)

We observed the following patterns across our sensor fleet:

Clean air: When the concentration of airborne particulates is below $10 \mu\text{g m}^{-3}$, the disparity between AQI_1 and AQI_2 predominantly clusters around zero, as indicated by a median value of $0.3 \mu\text{g m}^{-3}$. Within this concentration range, no bias is present, suggesting that the air quality measurements are consistent.

Dust burst: Between the hours of 14:45 and 18:35, the readings closely align; however, AQI_2 tends to slightly underreport the highest peaks. The sensors exhibit a deviation of approximately 15%, which falls within the acceptable tolerance range of $\pm 10 \mu\text{g m}^{-3}$, thus affirming the sensor kits' suitability for deployment.

Early drift: The observed 14-day slope is $+0.2 \mu\text{g/m}^3/\text{week}$ (with a p-value of 0.16), indicating a statistically non-significant

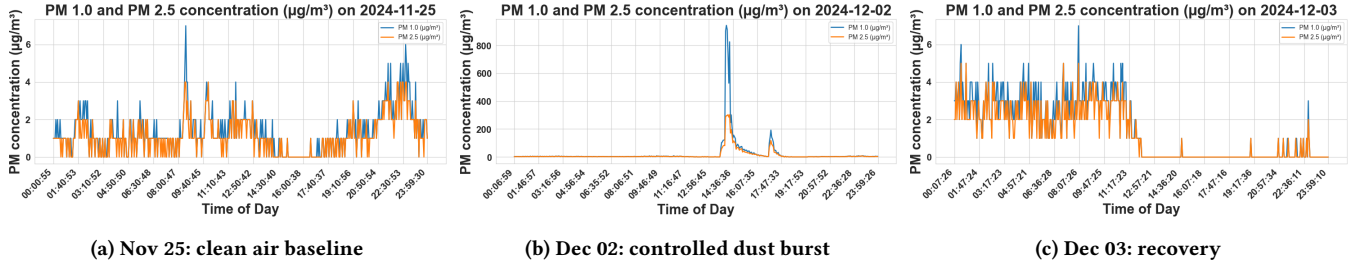


Figure 4: Four-stage calibration sequence for AQI_1 (mass concentration, $\mu\text{g m}^{-3}$). Phase 1 establishes the noise floor: 30-min $\sigma = 0.02 \mu\text{g m}^{-3}$, with all 1-min means $< 0.05 \mu\text{g m}^{-3}$. Phase 2 reaches a peak of $6 \mu\text{g m}^{-3}$, full-width-half-max ≈ 9 min. Phase 3 decays exponentially with $\tau \approx 11 \pm 1.3$ min finishing inside the $\pm 10 \mu\text{g m}^{-3}$ repeatability band.

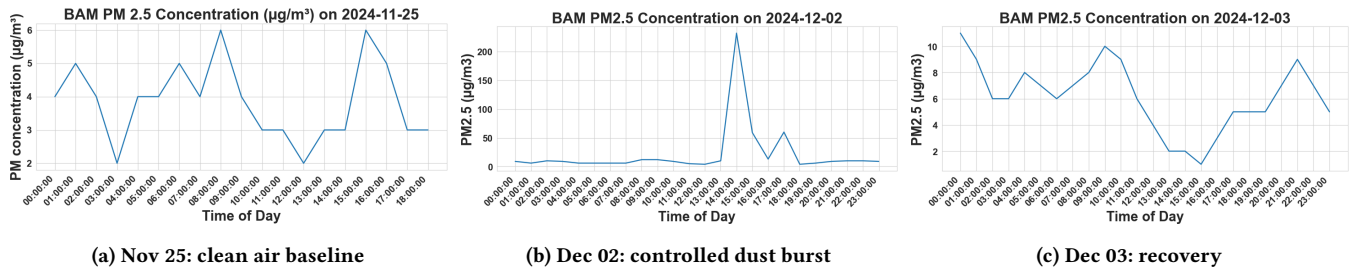


Figure 5: Hourly $\text{PM}_{2.5}$ concentrations measured by the reference BAM during the three key stages of the chamber calibration. (a) Typical background on November 25 stays near $2-6 \mu\text{g m}^{-3}$, defining the zero offset for the low-cost sensors. (b) On December 02, a 45-minute dust injection drives the BAM to a peak of $\sim 240 \mu\text{g m}^{-3}$, providing the span point. (c) By the next day (December 03), concentrations have fallen back to $1-11 \mu\text{g m}^{-3}$, confirming full purge of the chamber. These traces serve as the ground truth for the low-cost sensor in Fig. 4.

trend. Initial evaluations reveal that both optical counters perform similarly, with no significant differences detected. Furthermore, the sampling frequency appears to have minimal impact on bias or drift. Nonetheless, prolonged deployment may uncover potential long-term aging effects of the instruments.

The Bland-Altman analysis of AQI_1 and AQI_2 shows that the worst-case scenario occurred on a dust burst day, with a mean bias of $+2.8 \mu\text{g m}^{-3}$ for $\text{PM}_{1.0}$ and limits of agreement (LoA) from -8.9 to $+14 \mu\text{g m}^{-3}$. $\text{PM}_{2.5}$ showed a mean bias of $+2.1 \mu\text{g m}^{-3}$ and LoA of -5.6 to $+9.9 \mu\text{g m}^{-3}$. On other days, the limits of agreement were narrower, ranging from -1.9 to $+2.6 \mu\text{g m}^{-3}$ for both PM types. The twin sensors showed consistent performance in clean and dusty conditions, indicating effective calibration. Data from clean-burst-purge cycles revealed strong correlations in readings and demonstrated the sensors' durability. These findings support objective O2.

6.3 Ambient and Internal Health

OpenAQ-Transit logs two auxiliary data streams alongside particulate matter (PM) data: four ambient channels (air temperature, relative humidity, atmospheric pressure, and sound) and four self-diagnostic channels (microcontroller unit temperature, battery voltage, RSSI, and note-queue). These streams are crucial for the evaluation goals outlined in section 5.

Objective A1 aims to collect time-aligned ambient data to identify PM peaks linked to events like bus departures or HVAC cycles.

Objective A2 focuses on keeping the battery voltage stable and the MCU temperature at an optimal level for the results to remain consistent within $\pm 10 \mu\text{g m}^{-3}$. Objective A3 records RH and temperature data to correct humidity biases, improving agreement with the BAM. Lastly, A4 specifies that any deviations in diagnostics will trigger a fault tag within one synchronization cycle.

Data from sensor kit x643 on December 5, 2024, reveals HVAC cycling causing temperature fluctuations between $5.5 - 8.0^\circ\text{C}$ and RH from 50% to 70%. Across 55 kits, temperature variation stayed under 0.5°C and RH variations were below 3%, ensuring consistency for objectives A1 and A3. The correlation between temperature and humidity, along with pressure variations, demonstrates the sensors' ability to capture both steady environmental trends and temporary disturbances.

Diagnostics data presented in Figure 6 from sensor kit x643 over 72 hours (December 8–10, 2024) showed MCU temperature below 45°C and stable battery voltage between 4.8 V and 4.95 V, meeting objective A2. During 14 days of testing, five LOW_TEMP alerts were logged, with all alerts reaching the maintenance dashboard within one hour, demonstrating effective fault detection per objective A4.

6.4 Stage II: Stress & Robustness (O4)

Subjecting the solar nodes to prolonged darkness reduced the battery voltage to 2.8 V, placing it in the Low SoC band (see Table 5). This resulted in GPS fix times increasing from 10 to 25 minutes and adjustments to sync intervals: outbound from 8 hours to 12 hours

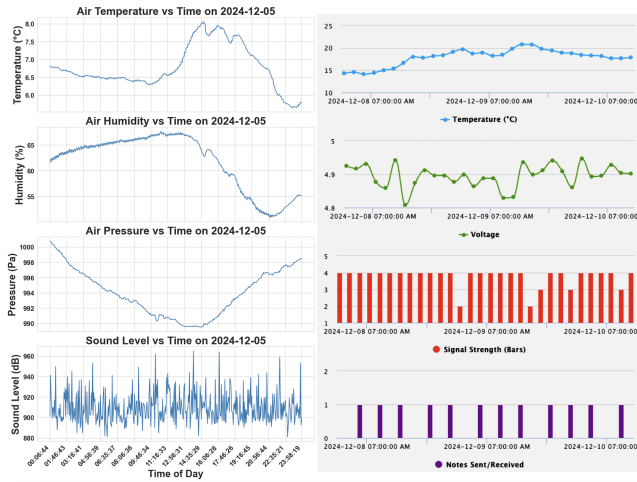


Figure 6: 24-hour record from a production kit (5 Dec 2024). Left column (a): Ambient air temperature, humidity, barometric pressure, and sound level provide context for explaining PM peaks (O1) and correcting O3 (humidity/temperature). Right column (b): MCU temperature, battery voltage, cellular RSSI, and Notehub message counts confirm safe thermal/power limits (O2) and enable quick fault detection via cloud diagnostics (O4). Across the fleet ($n = 55$), variations were minimal: 0.5 °C (air T), 3% RH, and 0.05 V (battery), indicating uniform performance before rollout.

Table 6: Stage-II fault-injection results (✓ = pass)

Test	Solar	USB	Metric verified
Deep-discharge	✓	—	V _{batt} , sync period
Cold-soak	✓	✓	xxxx_LOW_TEMP alert, recovery
Network blackout	✓	✓	queued notes, data-loss %
OTA update	✓	✓	uptake time, reboot persist
Drive test	—	✓	fix interval, backlog flush

and inbound from 4 hours to 8 hours. An alert xxxx_LOW_BATT was triggered. Once exposed to sunlight, the voltage rose to 3.2 V, allowing the system to revert to Normal SoC band intervals, as confirmed by texts and Notehub records.

In the cold-soak test, the xxxx_LOW_TEMP alert was triggered for all six nodes within 27 ± 3 minutes of entering the 5 °C chamber and cleared automatically upon warm-up. During OTA testing, the sensor window was updated from 4 to 5 minutes, and this change was successfully observed in the next polling cycle after synchronization.

While driving in clear skies, the sensor kits maintained GPS fixes but struggled during overcast conditions. During the modem blackout, each node buffered notes locally and uploaded them in the correct order once LTE was restored, ensuring no data loss. Table 6 summarizes the pass/fail outcomes for all fault injections.

These scenarios demonstrate the system's ability to maintain data integrity, self-regulate, and accept configuration updates in challenging conditions, addressing objective O4. The deep-discharge

test provided insights for drift analysis in objective O3, while continuous logging during temperature stress contributed to the stability dataset for objective O2.

7 Limitations

The identified limitations include reference co-location, where the gains and coefficients were derived from a 14-day chamber experiment utilizing a BAM. To address this, additional open-air co-location studies employing a TEOM or a similar gravimetric sampler are essential to account for variables such as roadside vibrations and weather variations. Furthermore, there is a concern regarding chemical specificity, as optical PM sensors are unable to distinguish between diesel soot and wind-blown dust. To tackle this issue, bench tests are being planned using a TGS5042 MOS CO sensor alongside an Alphasense NO₂-B43F electrochemical cell for source apportionment.

8 Conclusion

We introduced *OpenAQ-Transit*, a 55-node dual-mode air quality platform that integrates low-cost optical PM sensors with over-the-air managed software and firmware, along with an adaptive hybrid solar/vehicle power system. During a 14-day co-location period with BAM, the fleet achieved significant results. The accuracy was notable, with a span error within $\pm 15\%$ and a mean absolute error (MAE) of $\leq 2.8 \mu\text{g m}^{-3}$. In terms of resilience, the system demonstrated a cloud synchronization success rate of 99% and an impressive auto-recovery time from thermal and dust events of 11.0 ± 1.3 minutes. Furthermore, the efficiency was marked by an 88% reduction in fan and laser runtime with duty-cycled twin sensors, which exhibited no early drift.

Future work will involve a two-year deployment on routes served exclusively by electric buses, routes served only by diesel buses, and routes that utilize both types of buses in Nairobi and Kigali. The goal is to generate street-level pollution data and develop an aging curve for twin PMSA003I sensors in sub-Saharan traffic. Access to this exposure data is essential, as it enables transport agencies and NGOs to make informed decisions about fleet electrification and the design of low-emission zones.

Acknowledgments

We thank BasiGo Ltd. for providing access to electric buses in Nairobi and Kigali and student volunteers whose late-night soldering sessions transformed 55 kits from CAD files into field-ready hardware.

References

- [1] U.S. Environmental Protection Agency 2025. *Particulate Matter (PM) Basics*. U.S. Environmental Protection Agency. <https://www.epa.gov/pm-pollution/particulate-matter-pm-basics> Last updated 30 May 2025 – accessed 30 Jul 2025.
- [2] ArduCam. 2015. ArduCam Mini 2 MP Plus (OV2640) SPI Camera Module – board, datasheet, and wiring/schematic. Electronic component documentation. <https://www.arducam.com/arducam-2mp-spi-camera-b0067-arduino.html> Datasheet:https://www.uctronics.com/download/Amazon/ArduCAM_Mini_2MP_Camera_Shield_DS.pdf; Hardware application note (wiring & schematic): https://www.uctronics.com/download/Amazon/ArduCAM_Mini_2MP_Camera_Shield_Hardware_Application_Note.pdf. Accessed 2025-06-20.
- [3] Babatunde I. Awokola, Gabriel Okello, Kevin J Mortimer, Christopher P. Jewell, Annette Erhart, and Sean Semple. 2020. Measuring air quality for advocacy in Africa (MA3): feasibility and practicality of longitudinal ambient PM_{2.5}.

- measurement using low-cost sensors. *International Journal of Environmental Research and Public Health* 17, 19 (2020), 7243. doi:10.3390/ijerph17197243
- [4] Evangelos Bagkis, Theodosios Kassandros, and Kostas Karatzas. 2022. Learning calibration functions on the fly: hybrid batch online stacking ensembles for the calibration of low-cost air quality sensor networks in the presence of concept drift. *Atmosphere* 13, 3 (2022), 416. doi:10.3390/atmos13030416
- [5] Yun Cheng, Xiucheng Li, Zhiqiu Li, Shouxu Jiang, Yilong Li, Ji Jia, and Xiaofan Jiang. 2014. AirCloud: A cloud-based air-quality monitoring system for everyone. In *Proceedings of the 12th ACM Conference on Embedded Network Sensor Systems*. 251–265. doi:10.1145/2668332.2668346
- [6] Carolina Correia, Vânia Martins, Bernardo Matroca, Pedro Santana, Pedro Mariano, Alexandre Almeida, and Susana Marta Almeida. 2023. A low-cost sensor system installed in buses to monitor air quality in cities. *International Journal of Environmental Research and Public Health* 20, 5 (2023), 4073. doi:10.3390/ijerph20054073
- [7] Edimax. [n. d.]. AirBox: Smart Air Quality Detector with PM2.5 Temperature and Humidity Sensors. <https://www.edimax.com/> Accessed 18 Jun 2025.
- [8] Asamene Embiale, Feleke Zewge, Bhagwan Singh Chandravanshi, and Endalkachew Sahle-Demessie. 2019. Levels of trace elements in PM 10 collected at roadsides of Addis Ababa, Ethiopia, and exposure risk assessment. *Environmental Monitoring and Assessment* 191 (2019), 1–18. doi:10.1007/s10661-019-7503-3
- [9] Ken Gwilliam, Vivien Foster, Rodrigo Archondo-Callao, Cecilia Briceño-Garmendia, Alberto Nogales, and Kavita Sethi. 2008. The burden of maintenance: roads in sub-Saharan Africa. *AICD Background Paper* 14, 4 (2008). https://www.infrastructureafrica.org/system/files/BP14_Roads_maintxnew.pdf
- [10] Shu-Chiung Hu, You-Chiun Wang, Chiuan-Yu Huang, and Yu-Chee Tseng. 2009. A vehicular wireless sensor network for CO 2 monitoring. In *SENSORS, 2009 IEEE*. IEEE, 1498–1501.
- [11] Adafruit Industries. 2013. MicroSD Card Breakout Board+ (board, schematic, and EagleCAD files). Electronic component documentation. <https://www.adafruit.com/product/254> Schematic & tutorial download: <https://learn.adafruit.com/adafruit-micro-sd-breakout-board-card-tutorial/download>; EagleCAD PCB files: <https://github.com/adafruit/MicroSD-breakout-board>. Accessed 2025-06-20.
- [12] Adafruit Industries. 2015. BME280 Temperature, Humidity, and Pressure Sensor Breakout (board, schematic, and datasheet). Electronic component documentation. <https://www.adafruit.com/product/2652> Schematic & tutorial download: <https://learn.adafruit.com/adafruit-bme280-humidity-barometric-pressure-temperature-sensor-breakout/downloads>; Bosch BME280 datasheet: <https://cdn-learn.adafruit.com/assets/assets/000/115/588/original/bst-bme280-ds002.pdf?1664822559>. Accessed 2025-06-20.
- [13] Adafruit Industries. 2015. TCA9548A 1-to-8 I²C Multiplexer Breakout (board, schematic, and datasheet). Electronic component documentation. <https://www.adafruit.com/product/2717> Schematic & tutorial download: <https://learn.adafruit.com/adafruit-tca9548a-1-to-8-i2c-multiplexer-breakout/downloads>; Texas Instruments TCA9548A datasheet: <http://www.adafruit.com/datasheets/tca9548a.pdf>. Accessed 2025-06-20.
- [14] Adafruit Industries. 2022. PMSA003I Air-Quality Sensor Breakout (board and module datasheet). Electronic component documentation. <https://www.adafruit.com/product/4632> Sensirion PMSA003I module datasheet: https://cdn-shop.adafruit.com/product-files/4632/4505_PMSA003I_series_data_manual_English_V2.6.pdf. Accessed 2025-06-20.
- [15] Wan Jiao, Gayle Hagler, Ronald Williams, Robert Sharpe, Ryan Brown, Daniel Garver, Robert Judge, Motria Caudill, Joshua Rickard, Michael Davis, et al. 2016. Community Air Sensor Network (CAIRNSENSE) project: evaluation of low-cost sensor performance in a suburban environment in the southeastern United States. *Atmospheric measurement techniques* 9, 11 (2016), 5281–5292. doi:10.5194/amt-9-5281-2016
- [16] Sami Kaivonen and Edith C-H Ngai. 2020. Real-time air pollution monitoring with sensors on city bus. *Digital Communications and Networks* 6, 1 (2020), 23–30. doi:10.1016/j.dcan.2019.03.003
- [17] Miraal Kamal, Manal Atif, Hafsa Mujahid, Tamer Shanableh, Abdul-Rahman Al-Ali, and Ahmad Al Nabulsi. 2019. IoT based smart city bus stops. *Future Internet* 11, 11 (2019), 227. doi:10.3390/fi11110227
- [18] Federico Karagulian, Maurizio Barbiere, Alexander Kotsev, Laurent Spinelle, Michel Gerboles, Friedrich Lagler, Nathalie Redon, Sabine Cruniaire, and Annette Borowiak. 2019. Review of the performance of low-cost sensors for air quality monitoring. *Atmosphere* 10, 9 (2019), 506. doi:10.3390/atmos10090506
- [19] Patrick L Kinney, Michael Gatari Gichuru, Nicole Volavka-Close, Nicole Ngo, Peter K Ndiba, Anna Law, Anthony Gachanja, Samuel Mwaniki Gaita, Steven N Chillrud, and Elliott Sclar. 2011. Traffic impacts on PM2. 5 air quality in Nairobi, Kenya. *Environmental science & policy* 14, 4 (2011), 369–378.
- [20] Jason Jingshi Li, Boi Faltings, Olga Saukh, David Hasenfratz, and Jan Beutel. 2012. Sensing the air we breathe—the OpenSense Zurich dataset. In *Proceedings of the AAAI Conference on Artificial Intelligence*, Vol. 26. 323–325.
- [21] Di Liu, Qiang Zhang, Jingkun Jiang, and Da-Ren Chen. 2017. Performance calibration of low-cost and portable particular matter (PM) sensors. *Journal of Aerosol Science* 112 (2017), 1–10. doi:10.1016/j.jaerosci.2017.05.011
- [22] Balz Maag, Zimu Zhou, and Lothar Thiele. 2018. A survey on sensor calibration in air pollution monitoring deployments. *IEEE Internet of Things Journal* 5, 6 (2018), 4857–4870. doi:10.1109/JIOT.2018.2853660
- [23] Mamopeli Matoane and Roseanne Diab. 2003. Health risk assessment for sulfur dioxide pollution in South Durban, South Africa. *Archives of Environmental Health: An International Journal* 58, 12 (2003), 763–770. doi:10.3200/AEOH.58.12.763-770
- [24] Lamri Naidja, Hocine Ali-Khodja, and Salah Khardi. 2018. Sources and levels of particulate matter in North African and Sub-Saharan cities: a literature review. *Environmental Science and Pollution Research* 25 (2018), 12303–12328. doi:10.1007/s11356-018-1715-x
- [25] World Health Organization. 2021. *Air quality guidelines: global update 2021: particulate matter, ozone, nitrogen dioxide, and sulfur dioxide*. World Health Organization.
- [26] World Health Organization et al. 2016. Ambient air pollution: A global assessment of exposure and burden of disease. *Clean Air Journal* 26, 2 (2016), 6–6.
- [27] PurpleAir. 2025. *Technology: How PurpleAir sensors work*. PurpleAir LLC, Salt Lake City, UT, USA. <https://www2.purpleair.com/pages/technology> Accessed: Jun. 30, 2025.
- [28] Sarah Robertson and Mark R Miller. 2018. Ambient air pollution and thrombosis. *Particle and fibre toxicology* 15 (2018), 1–16. doi:10.1186/s12989-017-0237-x
- [29] Khaled F. Salama, Rashed F. Alhajri, and Abdulrahman A. Al-Anazi. 2017. Assessment of air quality in bus terminal stations in Eastern Province, Kingdom of Saudi Arabia. *Int. J. Community Med. Public Health* 4 (2017), 1413. doi:10.18203/2394-6040.ijcmph20171748
- [30] Sinan Sousan, Kirsten Koehler, Geb Thomas, Jae Hong Park, Michael Hillman, Andrew Halterman, and Thomas M Peters. 2016. Inter-comparison of low-cost sensors for measuring the mass concentration of occupational aerosols. *Aerosol Science and Technology* 50, 5 (2016), 462–473. doi:10.1080/02786826.2016.1162901
- [31] Seeed Studio. 2022. Grove – Loudness Sensor (board, schematic, and LM2904DR datasheet). Electronic component documentation. https://wiki.seeedstudio.com/Grove-Loudness_Sensor/ Schematic (Eagle v0.9b): https://files.seeedstudio.com/wiki/Grove-Loudness_Sensor/res/Grove%20-%20Loudness%20Sensor%20Eagle%20File_v0.9b.zip; LM2904DR datasheet: https://files.seeedstudio.com/wiki/Grove-Loudness_Sensor/res/LM2904DR.pdf. Accessed 2025-06-20.
- [32] R Subramanian, Abdou Safari Kagabo, Valérien Baharane, Sandrine Guhirwa, Claver Sindayigaya, Carl Malings, Nathan J Williams, Egide Kalisa, Haofan Li, Peter Adams, et al. 2020. Air pollution in Kigali, Rwanda: spatial and temporal variability, source contributions, and the impact of car-free Sundays. *Clean Air Journal* 30, 2 (2020), 1–15.
- [33] Péter Völgyesi, András Nádas, Xenofon Koutsoukos, and Ákos Lédeczi. 2008. Air quality monitoring with sensormap. In *2008 international conference on information processing in sensor networks (IPSN 2008)*. IEEE, 529–530.
- [34] Blues Wireless. 2023. Swan Feather-Compatible Microcontroller – Datasheet. <https://dev.blues.io/hardware/swan-datasheet/>. Accessed: 2025-06-20.
- [35] Blues Wireless. 2024. Notecarrier F Baseboard – Datasheet. <https://dev.blues.io/hardware/notecarrier-datasheet/notecarrier-f/>. Accessed: 2025-06-20.
- [36] Blues Wireless. 2025. Notecard Cell + WiFi (NOTE-WBGLW) – Datasheet. <https://dev.blues.io/datasheets/notecard-datasheet/note-wbglw/>. Accessed: 2025-06-20.
- [37] Blues Wireless. 2025. Notehub – Secure Data Routing Service for Notecard. Online platform documentation. <https://dev.blues.io/notehub/> Accessed 2025-06-20.
- [38] Kan Zheng, Shaohang Zhao, Zhe Yang, Xiong Xiong, and Wei Xiang. 2016. Design and Implementation of LPWA-Based Air Quality Monitoring System. *IEEE Access* 4 (2016), 3238–3245. doi:10.1109/ACCESS.2016.2582153